Marine Radar Image Sequence Target Detection Based on Space–Time Adaptive Filtering and Hough Transform

Baotian Wen, Zhizhong Lu, Yongfeng Mao, and Bowen Zhou

***Abstract*—The performance of marine radar target detection is largely affected by the intricate and dynamic space–time variations of sea clutter signals, which cause substantial numbers of false and missed alarms. To improve the target detection performance of rotating scanning marine radar, this study proposes a marine radar image sequence target detection algorithm based on space–time adaptive filtering and the Hough transform algorithm. The algorithm adopts a two-stage approach of coarse detection followed by precise detection. During the coarse detection stage, the sea clutter energy in the 3-D frequency–wavenumber spectrum of the marine radar image sequence is suppressed by a sea clutter suppression algorithm in the space–time domain, space–time clutter suppression (STCS). Subsequently, moving targets are extracted from the image sequence using a target energy extraction method based on the Hough transform algorithm in the 3-D frequency–wavenumber domain. The result is a processed image sequence with sea clutter signal reduction and target signal extraction. The precise detection stage detects the target point in this processed image sequence using a constant false alarm rate method based on a real clutter background distribution model. During verification tests on real X-band marine radar data, the detection probability of the proposed method reaches 99.89% under low sea state, 95.34% under medium sea state, and 94.44% under high sea state. Compared with the WHOS-CFAR and GMOS-CFAR, the average improvement is 10.1% and 16.6%, respectively. Furthermore, compared to the STCS, there is a maximum improvement of 3.7%. The enhancement in detection performance is significant.**

***Index Terms*—Constant false alarm rate, marine radar, radar image sequence, space–time adaptive filtering (STAF), target detection.**

I. Introduction

MARINE radar, which detects objects by emitting electromagnetic waves and receiving their echoes, operates continuously throughout the day and night. Marine radar is widely applied and plays a crucial role in tasks such as rainfall detection, wind field inversion, wave inversion, marine ecological protection, and maritime security defense [1], [2], [3], [4].

In marine radar signals radiated from the sea surface, the target information is combined with sea clutter information [5]. Sea clutter refers to the backscattering signals created when radar emitted electromagnetic waves scatter across the sea surface. Sea clutter is generated through complex physical mechanisms that depend on various factors, including the condition of the sea surface and oceanic meteorology. Consequently, sea clutter is characterized by highly intricate space–time variations. Moreover, the relatively diminutive size and intensity of marine-target signals in comparison to sea spikes make them easily overwhelmed by clutter signals [6]. Therefore, marine radar target detection against the complex background of sea clutter has always been a challenging and popular research topic.

The current target detection methods for marine radars can be classified into six main categories: traditional spatial domain processing, temporal domain processing, frequency domain processing, time–frequency domain processing, deep neural network learning, and space–time (frequency–wavenumber) domain processing.

Spatial domain processing analyzes the mechanism and characteristics of sea clutter using statistical methods. Various sea-clutter distribution models have been established, including the log-normal distribution, the Weibull distribution based on a multiparameter non-Gaussian model, the composite-model K distribution, and the generalized Pareto distribution of texture and speckle components based on a dual-scale model [7]. Multiparameter models can produce complex composite distributions that closely match the actual amplitude distributions of sea clutter. Under the appropriate radar parameters and sea surface conditions, each model achieves promising detection performance. However, sea clutter has non-Gaussian, nonlinear, and nonstationary properties, leading to notable variations in the amplitude distribution models of sea clutter across different time periods and sea areas [8].

Exploiting the self-similarity and scale invariance of sea clutter, temporal domain processing based on the fractal theory discriminates between sea clutter signals and target signals. Nevertheless, fractal techniques cannot detect swiftly moving targets and are considerably influenced by sea clutter [9].

Frequency domain processing methods include moving target indicator (MTI), moving target detection (MTD), eigenvalue decomposition (EVD), and singular value decomposition (SVD). The MTI and MTD methods employ cancelation filters between multiple consecutive pulses to separate the Doppler frequency shift that characterizes moving targets [10], [11]. The EVD

Manuscript received 20 April 2024; revised 23 June 2024; accepted 22 July 2024. Date of publication 29 July 2024; date of current version 8 August 2024. *(Corresponding author: Zhizhong Lu.)*

The authors are with the Harbin Engineering University, College of Intelligent Systems Science and Engineering, Harbin 150001, China (e-mail: 20130415@hrbeu.edu.cn; luzhizhong@hrbeu.edu.cn; myf_2021@hrbeu.edu.cn; s3220-40027@hrbeu.edu.cn).

Digital Object Identifier 10.1109/JSTARS.2024.3434358

and SVD methods adopt a subspace decomposition approach and exploit the first-order Bragg peak characteristic to suppress sea clutter energy in the frequency domain [12]. When the sea clutter is heavy, its first-order Bragg spectra broaden and overlap the Doppler frequency spectra of the targets, compromising the ability of these methods to suppress clutter and detect the targets.

Time–frequency domain processing methods exploit the dual benefits of the temporal and frequency domains. Target detection is based on the difference between the distinct distributions of sea clutter and target in the time–frequency domain [13]. The frequency aggregation location of the target signal is ultimately determined after different time–frequency transformations and searching for the optimal transform domain to estimate the target's motion parameters [14]. These methods adopt the short-time Fourier transform [15], fractional Fourier transform [16], or sparse Fourier transform [17]. Although time–frequency domain processing exclusively achieves energy accumulation, this advantage is limited to linear frequency modulation signals [14]. Deep neural network learning such as convolutional neural networks [18] and generative adversarial networks [19] process radar images from an image-processing standpoint. These methods autonomously learn and extract the features of the target signal in an image and perform tasks such as detection and segmentation [20]. Despite their promising performance and enormous potential [5], radar-target detection methods based on machine learning require a sufficient number of sample data from different sea conditions and target scenarios for the training process.

In the presence of heavy sea clutter and a low signal-to-clutter ratio (SCR), detecting an unknown number of targets in a single image is notoriously difficult. The performance of target detection can be improved using multiple radar images [21]. Unlike traditional target detection based on individual scans, space–time domain processing can jointly process the information in multiple consecutive scans to achieve robust detection [22]. Detection before tracking (TBD) and space–time adaptive filtering (STAF) belong to this class of methods. TBD synchronously integrates tracking and detection, avoiding the need for thresholding using the amplitude information, and accumulates multiple energies to enhance the target detection [23]. TBD for coherent radar includs Radon linear standard transform and so on [24], [25], [26]. TBD for noncoherent radar includs extended Kalman filter-based TBD, etc. [27], [28], [29]. Methods in the second category are based on the recursive Bayesian estimation framework. However, TBD methods require separate estimations of the target kinematics and modal states [30], whereas the shapes of real marine moving targets are typically irregular and variable.

STAF (frequency–wavenumber) domain processing such as space–time clutter suppression (STCS) [31], suppresses sea clutter by transforming a series of radar images into the frequency–wavenumber domain and constructing a filter based on the dispersion relation of the sea clutter energy. Although the STCS method effectively suppresses most of the sea spike signals in the original image sequence, there still exist a small number of heavy sea spike signals and noise signals in the processed image sequence. These clutter signals are scattered throughout the entire image, which cause false alarms in the subsequent precise detection stage. Therefore, in the coarse detection stage, this article proposes a novel clutter suppression method. After the STCS procedure, the 3-D frequency–wavenumber domain is transformed into the Hough detection domain to obtain specific information of the target frequency. According to the information, a space–time domain target extraction (STTE) procedure is established. The nontarget energy is further filtered by the process, including sea clutter and noise, thereby enhancing the SCR of the image sequence and reducing the presence of heavy clutter signals. As a result, the false alarm rate in subsequent precise detection is effectively decreased. In addition, within the STSC precision detection stage, a traditional sea clutter background distribution model is employed. The compound Gaussian distribution is utilized for offline fitting to ascertain the sea clutter distribution. However, even if the vast majority of sea clutter is suppressed, some rapidly changing sea spikes and attenuation effects on large spatial scales cause the distribution of background clutter to be nonstationary and non Gaussian. Consequently, a fixed fit distribution model cannot adequately replace real clutter distribution. This article proposes a novel real clutter background distribution constant false alarm rate (RCBD-CFAR) during precision detection stage. The background distribution model is dynamically updated in real time through the utilization of image sequences generated during the coarse detection stage, where the image sequence processed through sea clutter suppression, target removal, and attenuation suppression.

The rest of this article is organized as follows. Section II describes the modeling of sea clutter spectra and moving target spectra in the frequency–wavenumber domain. Section III presents the proposed space–time adaptive target detection algorithm. Section IV presents the experimental results. Section V discusses the proposed method, and finally, Section VI concludes this article.

II. Models for Sea-Clutter and Moving-Target Spectra in the 3-D Frequency–Wavenumber Domain

This section describes the spectral components of a marine radar image sequence in the 3-D frequency–wavenumber domain and overviews a validated sea clutter model. In addition, the distinctive features of moving targets in the 3-D frequency–wavenumber domain is elucidated, supports the subsequent processes of clutter suppression and moving target extraction.

A. Frequency Spectrum of Sea Clutter in the Frequency–Wavenumber Domain

The 3-D fast Fourier transform (3D-FFT) transforms a marine radar image sequence into an image spectrum in the 3-D frequency–wavenumber domain. An integration image along the θ-direction in the spectral domain obtained from a set of radar image sequence is shown in Fig. 1. It should be noted that Fig. 1 is derived directly from the actual measured radar image sequence without target. The image spectrum comprises static and quasistatic energy spectra [32], the frequency spectrum of a stationary or slowly moving target, the characteristic frequency

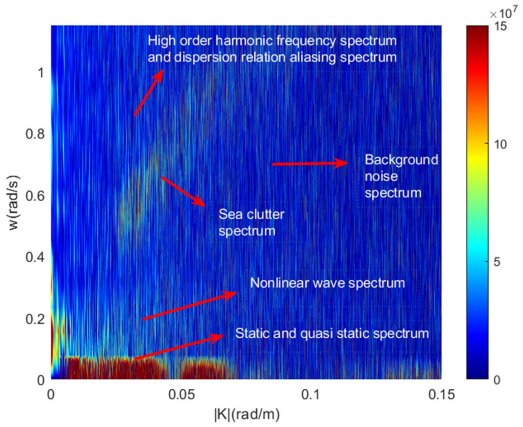

Fig. 1. Integrated image along the θ-direction in the 3-D frequency–wavenumber spectral domain $V_{\omega,k}$ corresponding to the radar image sequence.

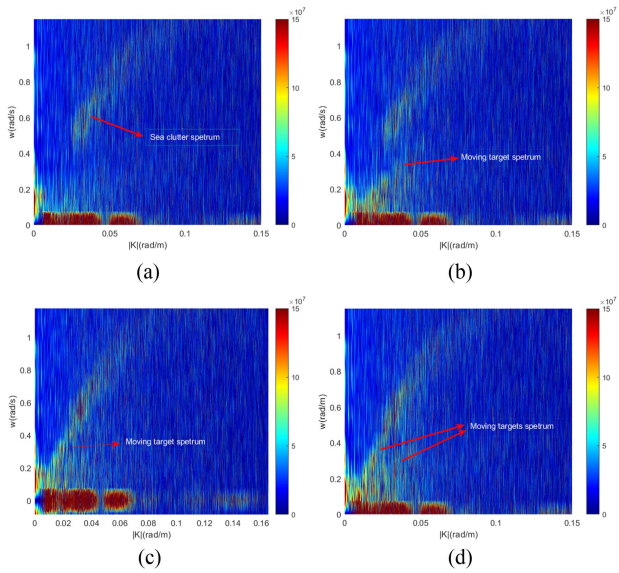

Fig. 2. Integration image along the θ-direction in the 3-D frequency–wavenumber spectral domain $V_{\omega,k}$ of (a) pure sea clutter with no target, (b) one target moving at 10 m/s, (c) one target moving at 15 m/s, and (d) two targets, one moving at 10 m/s and the other moving at 15 m/s.

spectrum of nonlinear waves, the high-order harmonic frequency spectrum, the aliased energy spectrum based on the fundamental dispersion relation curve, and the frequency spectrum of the background noise [33].

Marine radar image sequences cover an enormous spatial scale over a short temporal scale. Therefore, the wave field and flow field within these sequences can be assumed as spatially homogeneous and temporally stationary. In such cases, sea clutter in the frequency–wavenumber domain exhibits first-order gravity wave characteristics, and the spectrum is concentrated near the basic dispersion relationship curve [34].

$$\omega = \sqrt{g \cdot k \cdot \tanh(k \cdot h)} + \vec{k} \cdot \vec{u} \tag{1}$$

where ω is the frequency of sea gravity wave, g is the gravitational acceleration, h is the water depth, k is the modulus of the wave number, $\vec{u} = (u_x, u_y)$ is the sea current direction relative to the ship, and $\vec{k} = (k_x, k_y)$ is the wavenumber vector.

The basic dispersion relation satisfied by first-order gravity waves is accompanied by higher order dispersion relations satisfied by higher order gravity waves. The higher order dispersion relations are defined as

$$\omega = (p+1)\sqrt{g \cdot k \cdot \frac{1}{p+1} \cdot \tanh\left(\frac{k \cdot h}{p+1}\right)} + \vec{k} \cdot \vec{u} \tag{2}$$

where $p = 0, 1, 2 \ldots$, is an order variable primarily reflecting the differences among different order dispersion relations. When $p = 0$, the basic linear dispersion relation is obtained, whereas for $p \neq 0$, a pth-order nonlinear dispersion relation is obtained.

B. Frequency Spectrum of the Moving Target in the Frequency–Wavenumber Domain

Irregular waves composed of waves with different frequencies separate into their component waves during propagation. Frequency dispersion is driven by the different periods and corresponding velocities of the component waves. In deep water, the wave velocity and period are related as follows:

$$v_i = \frac{\lambda_i}{T_i} = \frac{gT_i}{2\pi} \tanh k_i h \tag{3}$$

where v_i, λ_i, T_i, and k_i represent the wave velocity, wave length, wave period, and wave number, respectively, of the individual wave i in the spectrum of the moving target.

The higher velocity waves are trailed by the lower velocity waves. Whereas sea clutter comprises waves of different frequencies and follows the dispersion relationship, the constituent points of targets within marine radar images can be regarded as moving uniformly and linearly at the same velocity. Therefore, the target points disobey the dispersion relationship and can be treated as a single large point. Scanning marine radars cannot rapidly accumulate pulses over a short period. However, the targets motions of targets within scanning radar images can be considered as slow linear movements that are displaced by limited amounts in multiple images, enabling the accumulation of multiple pulses. The velocity of the target can then be computed considering the Doppler-frequency shift properties between the spectra. In the frequency–wavenumber domain, the large point described previously consists of composite frequencies with very similar wave velocities and periods. Consequently, in the radar image sequence, the frequency spectrum of the uniformly moving target comprises a group of similar frequencies with nearly constant wave velocities. The wave velocity and ω are related as

$$\omega_i = |k_i| \cdot v_i \tag{4}$$

where ω_i is the frequency of the sea gravity wave and $|k_i|$ is the modulus of the wave number of individual wave i in the moving-target spectrum.

Fig. 2 presents integrated images along the θ-direction in the 3-D frequency–wavenumber spectrum domain, depicting both moving targets with constant velocities and pure sea clutter. Furthermore, Fig. 2 is generated by combining the radar image sequence without target and the target sequence extracted from

the radar image sequence with target, both of which are based on actual measurement data. The slopes of the target frequency spectra depicted in Fig. 2(b)–(d) correlate with the velocities of the corresponding targets. Prominent spectral features of the target frequency spectrum appear in the $|K| - w$ domain, but the angle and phase information of the wavenumber domain is absent. Consequently, crucial directional information on the target motion is lost and the targets in multitarget scenarios are not easily differentiated and extracted. To overcome these limitations, a 2-D cross section can be obtained from the 3-D frequency–wavenumber image spectrum along the ω-direction, where k_x (v_x) and k_y (v_y) represent the wavenumber (velocity) components of the target along the X- and Y-directions in the wavenumber domain, respectively. The following equation is derived:

$$k_{iy} = -\frac{v_{ix}}{v_{iy}} \cdot k_{ix} + \frac{\omega_i}{v_{iy}}. \tag{5}$$

An image captured via a scanning radar requires a complete circle scan, which considerably extends the time interval. Consequently, the corresponding values in the image sequence are inherently discrete. In this scenario, the moving target frequency spectrum appears as a series of straight lines corresponding to the discrete frequencies in the wavenumber domain corresponding to each discrete frequency ω. The slope of each line is determined by v_{ix} and v_{iy}. The X and Y intercepts in the wavenumber domain are determined by the wave velocities of the target spectra and the discrete ω values corresponding to the wavenumber domain. Meanwhile, the target frequency spectrum on the zero-frequency plane ($\omega = 0$) invariably intersects the origin. In the case of staring radar, the time interval of image acquisition is small and ω is approximately continuous. The target spectrum in the 3-D frequency–wavenumber domain then manifests as a plane passing through the central point. The normal vector of this plane is determined by the orientation and magnitude of the wave velocity associated with the target frequency.

The 1st and the 32nd original images in a set of image sequences are depicted in Fig. 3(a) and (b), respectively, with an interval time of 80 s. These images contain four targets moving approximately in a straight line at uniform speed. Specifically, the first target moves at an angle of 57° with respect to due north, the second target moves at an angle of 45° with respect to due north. The third target moves at an angle of 90° with respect to due north, while the fourth target moves at an angle of 0° with respect to due north. Due to the decrease in target frequency as ω deviates from 0, the energy in the images before the 9th and after the 25th diminishes to an undetectable level. Consequently, any two images between the 9th and 25th are selected to calculate variations in moving target frequency within the 3-D frequency–wavenumber domain. Fig. 3(c)–(e) displays the 10th ($\omega = 0.54978$), 16th ($\omega = 0.07854$), and 17th ($\omega = 0$) 2-D cross sections along the ω-direction in a 3-D spectral domain $V_{\omega,k}$ with four moving targets. The four targets move uniformly and linearly in different directions (57°, 45°, 90°, and 180° with respect to due north) within 80s. The zero-frequency plane [17th spectrum; Fig. 3(c)] contains numerous frequencies that gradually attenuate over distance and stationary object frequency.

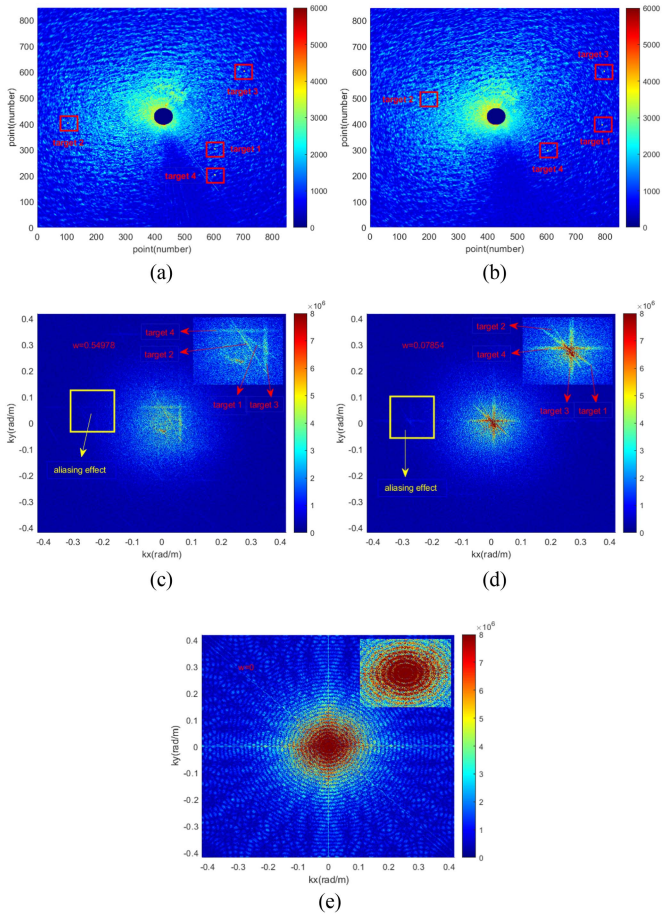

Fig. 3. First and the 32nd images in a set of image sequences. (a) First original image, and (b) 32th original image. 2-D cross sections along the direction in a 3-D spectral domain $V_{\omega,k}$ with four targets. (c) Tenth spectrum ($\omega = 0.54978$), (d) 16th spectrum ($\omega = 0.07854$), and (e) 17th spectrum ($\omega = 0$) in the frequency–wavenumber domain.

Owing to the colossal spatial-temporal scale of electromagnetic wave attenuation across the entire radar image, the distribution is concentrated around the zero-frequency domain. A pronounced proportion in this plane is acquired by the dc component of the sea clutter. Combining the 10th and 16th spectra, the spectra of the four target frequencies clearly change with target velocity and direction. As ω increases, the target frequency moves in the same direction as the target movement in space–time domain, manifested as the translation of a straight line. In addition to the predominant frequency spectra conforming to (5), a limited number of frequency spectra satisfy only the slope requirement, violating the intercept condition. These spectra actually originate from aliasing effects, some of these are marked in the yellow box. The conditions for aliasing effects are as follows:

$$dk_m = \frac{2\pi}{L_m} = \frac{2\pi}{v_m} \cdot dt \cdot \text{num} \tag{6}$$

$$v_m \cdot dt \cdot num = n \cdot dm \tag{7}$$

where dk_m, L_m, and V_m represent the wavenumber resolution spatial displacement scale, and movement velocity, respectively, of the target, dt is the temporal resolution of radar sampling,

num is the number of images in the radar image sequence, n is the total number of points of the target moving through the spatial domain, and d_m is the spatial resolution of the target. The wavenumber of the target is then derived as

$$k_m = \frac{2\pi}{dm}. \tag{8}$$

The target frequency ω_m can be obtained from the velocity of (4) and the aliasing conditions are determined using the Nyquist sampling theorem $\omega \geq 2\omega_m$, which is represented as $n \geq 2 \cdot \text{num}$. According to (8), aliasing is avoided when the distance moved by the target between two consecutive radar images is less than twice the unit distance. In addition, if the target between two successive radar images is displaced by less than the resolution of the unit distance, its motion will be undetected, and subsequently, classified as stationary. Owing to the limited temporal resolution and high spatial resolution of marine radar, spectral aliasing in the frequency domain is inevitable for real moving targets.

C. Distribution Model of the Real Clutter Background

CFAR detection under sea clutter background is a traditional method for sea surveillance radar target detection. Surrounding environmental factors such as wind speed, temperature, attenuation effects, and target signals introduce large space–time variations in distribution models of sea clutter [35]. The original image sequence undergoes the sea clutter suppression (see Section III-A) and target removal (see Section III-B), the image sequence with sea clutter suppression, target removal and attenuation suppression is obtained. By counting all signals in the processed image sequence, a stable and real clutter background distribution (RCBD) model can be obtained. The process of obtaining this distribution is explained in detail in Section III-C.

The RCBD model differs from the traditional compound Gaussian (CG) distributions such as the Weibull and log-normal distributions (which are special forms of the CG distribution), and the K, Pareto, and CG inverse Gaussian distributions, in terms of different statistical objects and different methods of acquisition. In the traditional distribution model, the statistical object is the sea clutter background data. A significant volume of authentic sea clutter background data is counted in an offline manner. Subsequently, various GC distribution models are employed to accurately fit the distribution model of the sea clutter background data. The resultant fitting outcomes are then utilized to ascertain the most suitable distribution model that can effectively replace the actual sea clutter background distribution model. The resulting statistics in RCBD model are no longer based on the original sea clutter background, but rather on the processed clutter background. By virtue of the two filtering steps, the RCBD model can seamlessly substitute the distribution model of the real clutter background. This substitution not only facilitates online acquisition but also obviates the necessity for fitting composite Gaussian distribution models.

Fig. 4 illustrates the distribution curves of various types of background clutter under different conditions. As the intensity of the sea state increases, the overall distribution of the original sea clutter background tends to concentrate toward elevated grayscale values. These fixed distribution models are best suited to particular sea surface environmental conditions. Alterations to these conditions can rapidly deteriorate the fittings of these distribution functions to the actual circumstances. The RCBD model (black dashed curves in Fig. 4) resolves the problems caused by intense space–time variations. It remains unaffected by environmental variables such as temporal lapse and sea conditions, enabling real-time acquisition of varying background clutter models, and it exhibits exceptional stability.

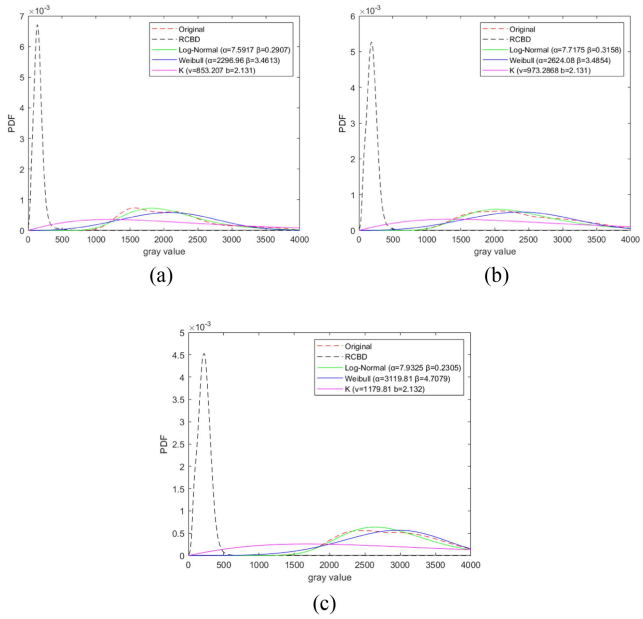

Fig. 4. Original sea clutter distribution, RCBD (the clutter background distributions obtained by sea clutter suppression and target removal), logarithmic normal, Weibull, and K distribution fittings to the original radar image sequence under (a) low sea conditions, (b) medium sea conditions, and (c) high sea conditions.

III. Target Detection Based on STAF

This section introduces the proposed target detection algorithm. Fig. 5 shows the architecture of the method. First, the disruptive effects of sea clutter are suppressed through an STCS filter on the interpolated image sequence. Subsequently, the energy of target is extracted by the STTE filter on the sea clutter suppressed image sequence. In this coarse detection process, target extracted image sequence and sea clutter suppression, target removal, and attenuation suppression image sequence is obtained. Thereafter, RCBD model is applied to precise detection.

A. Sea Clutter Frequency Suppression Segment

The STCS filter is employed for mitigating sea clutter in coarse detection. The marine radar image sequence $\eta(x, y, t)$ is 3D-FFT-transformed to a 3-D frequency–wavenumber spectrum $F(k_x, k_y, \omega)$. The discrete form of this spectrum is expressed as

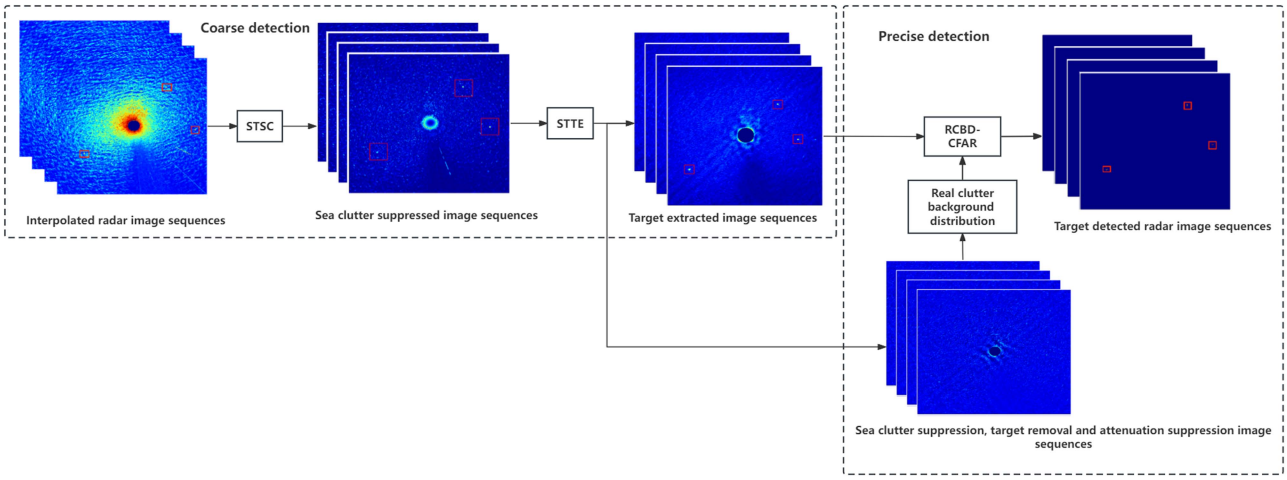

Fig. 5. Architecture of target detection in a marine radar image sequence based on STAF and the Hough transform.

follows:

$$F(k_x,k_y,\omega)=\sum_{0}^{L_y}\sum_{0}^{L_x}\sum_{0}^{T}\eta(x,y,t)\exp\left[-2\pi i\left(k_x x/L_x+k_y y/L_y+\omega t/T\right)\right] \quad (9)$$

$$I(k_x,k_y,\omega)=\frac{1}{L_xL_yT}\left|F(k_x,k_y,\omega)\right|^2 \quad (10)$$

where L_x and L_y are the spatial scales of the image sequence, and T denotes the temporal scale. k_x and k_y denote the wavenumber components of the spectrum, ω is the temporal frequency, and $I(k_x,k_y,\omega)$ is the 3-D frequency–wavenumber image spectrum. The resolutions of the wavenumber components and frequency are $dk_x=\frac{2\pi}{L_x}$, $dk_y=\frac{2\pi}{L_y}$, and $d\omega=\frac{2\pi}{T}$.

The 2-D wavenumber modulation frequency spectrum $I(|K|,\omega)$ is obtained by integrating $I(k_X,k_y,\omega)$ over the wavenumber angles. The module of all points with values exceeding 0.95^*C in the spectrum (where C is the calculated maximum spectral value) are averaged to obtain the leading wavelength $|K_m|$ of the waves. The upper and lower boundaries of the filter are then determined from $|K_m|$ and the maximum relative velocity $|U_{\max}|$ as follows:

$$|K_p|=\frac{\left(\omega+\frac{d\omega}{2}+|K_m|\cdot|U_{\max}|\right)^2}{g}+\frac{dK}{\sqrt{2}} \quad (11)$$

$$|K_n|=\frac{\left(\omega-\frac{d\omega}{2}-|K_m|\cdot|\mathrm{U}_{\max}|\right)^2}{g}-\frac{dK}{\sqrt{2}} \quad (12)$$

where $|K_p|$ and $|K_n|$ refer to the upper and lower boundaries of frequency band of the filter, respectively.

The STCS model obtained by (13) and (14) as follows:

$$E(k_x,k_y,w)=\begin{cases}0 & w\in[K_n,K_p]\\ I(k_x,k_y,w) & \text{else}\end{cases} \quad (13)$$

where $E(k_x,k_y,\omega)$ represents the sea clutter suppression image spectrum.

The energy of the targets is distributed across the entire $I(k_x,k_y,\omega)$ domain and is largely concentrated below 0.4712 rad/s, meanwhile, the energy rapidly increases with decreasing ω. Specifically, 87.26% of the target energy is concentrated in the 0 to 0.3142 rad/s range of ω. Consequently, the filtering out of high value ω intervals does not adversely affect the target energy. The $[K_n,K_p]$ bandwidth is positively correlated with ω, indicating that the bandwidth interval decreases with decreasing ω. Within the 0 to 0.3142 rad/s range of ω, the bandwidth ranges from 0.059 to 0.078 rad/s. In this scenario, the target energy is completely removed only when the wave-velocity range of the target falls entirely within the interval boundaries, i.e., $V_m\in[K_n/K,K_p/K]$. However, the interval bandwidth of the target energy (0–0.157 rad/s) is not entirely encompassed by the filtering interval. Therefore, when the STCS filtering method removes energy within the range $\omega\in[K_n,K_p]$, it preserves most of the energy associated with the real targets but inevitably removes a small portion of that energy.

B. Target Frequency Extraction Segment

The number of moving target points in radar images is much lower than the number of sea clutter points. Consequently, most of the signals collected from an image belong to sea clutter. The small volume of target signals causes a considerable energy disparity between the sea clutter spectrum and the moving target spectrum in the 3-D frequency–wavenumber domain, obscuring the frequency spectrum of the moving target. After sea clutter suppression segment, the sea clutter frequency in the spectrum is substantially reduced and the frequency of moving target becomes easily identified and detected. The frequency shift of the moving target remains stable over multiple scanning periods. The frequency spectrum of the target on all wavenumber planes is then calculated by measuring the frequency shift generated between the two wavenumber planes corresponding to ω. This calculation uses the wavenumber planes near the zero-frequency–wavenumber plane, because the frequency spectrum of the moving target always passes through the origin in the

3-D frequency–wavenumber domain. In this article, the target frequency spectrum is extracted from the 16th and 18th images ($\omega = 0.07854$ and -0.07854) rather than the zero-frequency–wavenumber plane, as the latter contains a considerable amount of static, quasistatic spectrum, and background noise. To reduce the computational time and eliminate the aliasing effect in the entire image spectrum, the central region $E(k_x^{1:i}, k_y^{1:i}, \omega)$ of the aforementioned two wavenumber planes is extracted.

The target spectrum was detected using the Hough detection method based on the duality between points and lines [36]. A line in Cartesian coordinates is represented by its slope K and intercept b, which correspond to the length of its perpendicular ρ from the origin and the angle θ between the perpendicular line and x-axis, respectively, in Hough space. A line passing through a point $A(x_a, y_a)$ in the plane is represented by a curve α in the Hough space, while a line passing through two points $A(x_a, y_a)$ and $B(x_b, y_b)$ is represented as the intersection of two curves α and β in the Hough space, where curve β corresponds to a line passing through point $B(x_b, y_b)$, in the plane. Thus, the problem of line existence is transformed into the problem of curve intersection. The intersection points of curves α and β are, respectively, determined as

$$\rho = x_a \cdot \cos\theta + y_a \cdot \sin\theta \tag{14}$$

$$\rho = x_b \cdot \cos\theta + y_b \cdot \sin\theta. \tag{15}$$

A binary transformation is performed on $E(k_x^{1:i}, k_y^{1:i}, \omega)$ and an accumulation array $H[\rho, \theta]$ is established in the ρ and θ parameter spaces. For each point (x, y) represented by 1 in the binary image, each possible value on the θ-axis sampled and its corresponding value ρ is calculated and accumulated in the array. The local peak in the accumulated array of ρ and θ values is then detected to determine the Hough parameters of the detected line.

The two line with the same angle θ in the Hough parameters of the two selected wavenumber planes are assigned to the same class, and the ρ difference between each pair of lines within the same class is calculated to obtain the frequency shift information. Leveraging this information, a model of the line spectrum on all wavenumber planes for each ω can be derived. The width of the line spectrum in the frequency–wavenumber domain is dictated by the scale of the target; specifically, a wider line spectrum corresponds to a larger spatial scale. However, the actual target spectrum on each wavenumber plane is not a singular line spectrum but consists of multiple line spectra. The width of the line spectra must be expanded when extracting the spectrum. This approach extracts most of the target spectrum while accepting a small part of the clutter spectrum, achieving robust processing performance even in scenarios involving multiple similar moving targets. The STTE model is finally derived as follows:

$$M(k_{x,w}, k_{y,w}, w) = \begin{cases} E(k_x, k_y, w) & k_{y,w} = K_r \cdot k_{x,w} + b_{w,r} \\ 0 & \text{else} \end{cases} \tag{16}$$

$$b_{\omega,r} = \left(\frac{b_{\omega_a} - b_{\omega_b}}{a - b}\right) \cdot (a - n) + b_{\omega_a} \pm C_i \tag{17}$$

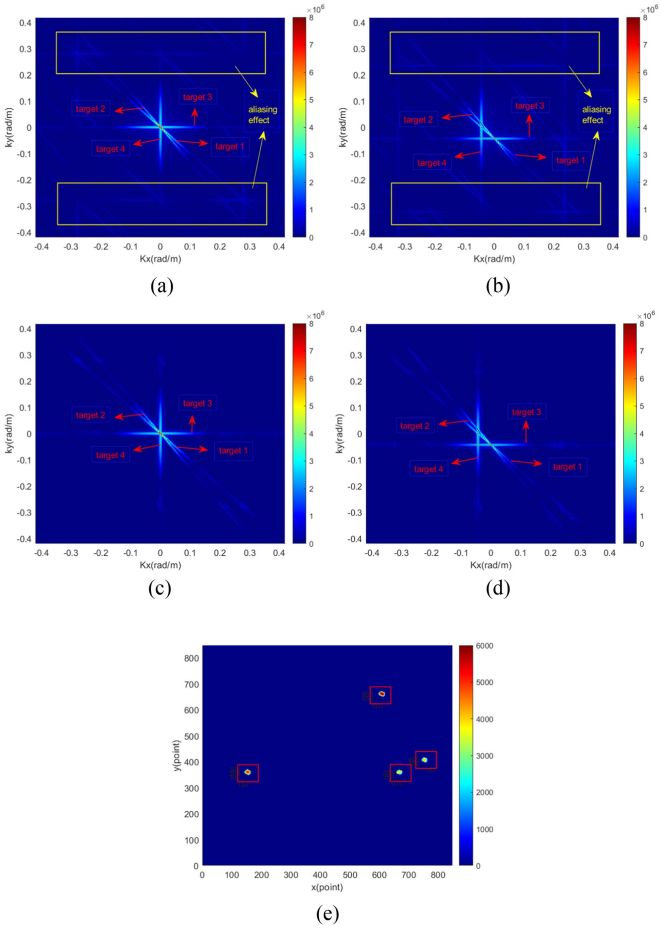

Fig. 6. 2-D cross section in the 3-D image spectral domain $V_{\omega,k}$ along the ω-direction. (a) Tenth cross-sectional spectrum and (b) 16th cross-sectional spectrum. The spectrum filtered by the Hough transform. (c) Tenth cross-sectional spectrum, and (d) 16th cross-sectional spectrum. The image sequence corresponds to the spectrum after Hough transform filtering. (e) 18th image.

where K_r and $b_{\omega,r}$ represent all line slopes and intercepts separately detected by the Hough transform. n represents the index of a wavenumber spectrum in the frequency–wavenumber domain, a and b represent the sequence numbers of the two selected images, and C_i is the width expansion coefficient.

In order to clearly show the influence of the Hough transform on target spectrum extraction, a set of original target image sequences (consisting of only four targets with the same characteristics as those in Fig. 3) are utilized to present the target spectrum and the spectrum filtered by Hough transform, as depicted in Fig. 6(a)∼(e). From the result, Hough transform can accurately capture the variation pattern (moving direction and speed) of target frequency in the 3-D frequency–wavenumber domain. During the process, a portion of the target spectrum energy generated by the aliasing effect was discarded, and only the target spectrum energy without aliasing was retained. Simultaneously, $C_{\max}$ is selected as the maximum width of C_i, and its selection affected the filtering results. A larger $C_{\max}$ resulted in less loss of energy from the target spectrum, while a smaller value has an opposite effect. During the process of $C_{\max}$ from 0 to 5, there was a significant improvement in the average extracted

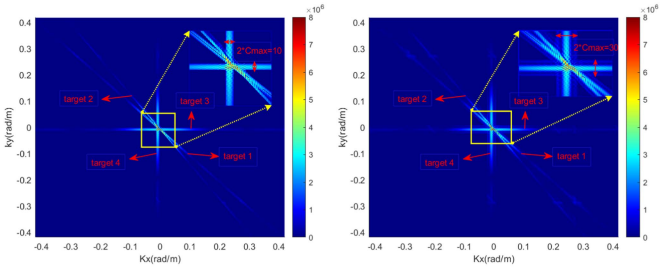

Fig. 7. STTE filter model in the 18th 2-D cross-sectional spectrum of 3-D image spectral domain under different $C_{\max}$ values. (a) $C_{\max}$=5 and (b) $C_{\max}$=15.

energy of the target frequency increasing from 0% to 68.95%, due to main frequency width being approximately 0.0148 rad/m (about five resolution units wide). As $C_{\max}$ ranges between 5 and 23, it had steady enhancement in average extraction energy of the target frequency reaching up to 84.22%. Although the extraction rate was higher in the range of 15–23, it also leaded to substantial enhancement in extraction energy of clutter. Thus, $C_{\max}$ in this range was not being selected. After $C_{\max}$ reaches 23, the enhancement rate decreased significantly and reached 100% at around 210. This phenomenon arises from the remaining target energy dispersed across entire frequency–wavenumber domain as aliasing energy form. In this article, $C_{\max}$ was selected as 15 to ensure that the final extraction result contained less clutter spectrum energy while maximizing the target spectrum energy extraction. Fig. 6(e) depicts the 18th image of filtered radar image sequence (enlarged target size), with an average extraction energy of 78.57% for four targets. In addition, certain clutter points around the targets appeared after Hough transform that require further elimination in the subsequent precision detection segment. The Hough transform extraction results with $C_{\max}$=5 and $C_{\max}$=15 are shown in Fig. 7(a) and 7(b).

After suppressing the sea clutter and extracting the target from the frequency–wavenumber spectrum, $M_c(k_x, k_y, \omega)$ is processed through a 3-D inverse fast Fourier transform (3D-IFFT) to obtain an image sequence

$$\eta_m(x,y,t) = \frac{1}{L_y}\frac{1}{L_x}\frac{1}{T}\sum_{0}^{L_y}\sum_{0}^{L_x}\sum_{0}^{T} M_c\left(k_x,k_y,\omega\right)\exp\left[2\pi i\left(k_x x/L_x + k_y y/L_y + \omega t/T\right)\right]. \quad (18)$$

C. Precise Detection Stage

The sea clutter suppression and target extraction segments retain a substantial portion of the target signals in the radar image sequence, along with a minor portion of background clutter signals. The clutter signals are preserved because the width expansion applied during target extraction inevitably includes nontarget spectra. Consequently, the detection of the $\eta_m(x,y,t)$ image sequence must be refined for ultimate target detection. The real clutter background spectrum P is obtained by removing the sea clutter and target spectra from spectrum I. The RCBD model is then obtained via IFFT as follows:

$$P\left(k_x,k_y,\omega\right) = M_c\left(k_x,k_y,\omega\right) - M_t\left(k_x,\mathrm{k}_y,\omega\right) \quad (19)$$

$$\eta_c(x,y,t) = \frac{1}{L_y}\frac{1}{L_x}\frac{1}{T}\sum_{0}^{L_x}\sum_{0}^{L_y}\sum_{0}^{T} P\left(k_x,k_y,\omega\right)\exp\left[2\pi\left(k_x x/L_x + k_y y/L_y + \omega t/T\right)\right] \quad (20)$$

where $P(k_x, k_y, \omega)$ and $\eta_c(x, y, t)$ denote the spectrum and distribution of the background clutter, respectively.

M_t and M_c were obtained by selecting different $C_{\max}$ values from (16) and (17), respectively. The C_t corresponding to M_t is smaller than the C_c corresponding to M_c, with C_t and C_c determined by experiments as 5 and 15, respectively. Consequently, the spectrum extracted from M_c exhibits more target frequency and background clutter frequency compared to that of M_t. In (18), M_c is utilized in order to obtain the processed image η_m with sea clutter suppression, target extraction, and attenuation suppression. On the other hand, M_t is utilized in (19), which effectively eliminates a significant portion of target frequencies present in M_c. Through (20), the RCBD model η_c is derived. The η_c can serve as a real time background clutter image of η_m.

η_c is an amplitude distribution rather than a complex number distribution. In addition, it is obtained by statistically processing the real-time background clutter through sea clutter suppression and target removal. In the sea clutter background distribution model CFAR method, to maintain the CFAR capability of the detector, the relationship between false alarm rate P_{fa} and the normalization factor τ must be established using the distribution model and decision rule. Once the desired P_{fa} is defined, the normalization factor τ is typically obtained through offline calculations conducted in advance, a set of reference units in close proximity to the target unit is obtained online and the detection threshold is determined. The entire image is then scanned point-by-point using a sliding window. The aforementioned method can be improved by using (21) and (22). Because the distribution model accurately characterizes the clutter background (with the target removed), once the desired P_{fa} is specified, the detection threshold T of the entire image sequence can be determined without normalizing τ. The relationship between P_{fa} and T is provided in (21), where $f(x)$ is the PDF curve of η_c. Furthermore, the point-by-point sliding window approach transitions to a more efficient whole image sequence detection scheme that simplifies the implementation of the detection process. The specific detection way is illustrated in (22), where D is the image sequence to be detected, i is the ith image in the image sequence, n is the nth point in the image, and T is the detection threshold

$$1 - P_{\text{fa}} = 1 - \int_{T}^{\infty} f(x)dx = \int_{0}^{T} f(x)dx \quad (21)$$

$$D_i(n) \underset{H_0}{\overset{H_1}{\gtrless}} T. \quad (22)$$

If the grayscale value of detection point $D_i(n)$ exceeds the detection threshold, it is designated as a target point and denoted as H_1. Conversely, if the grayscale value falls below the detection

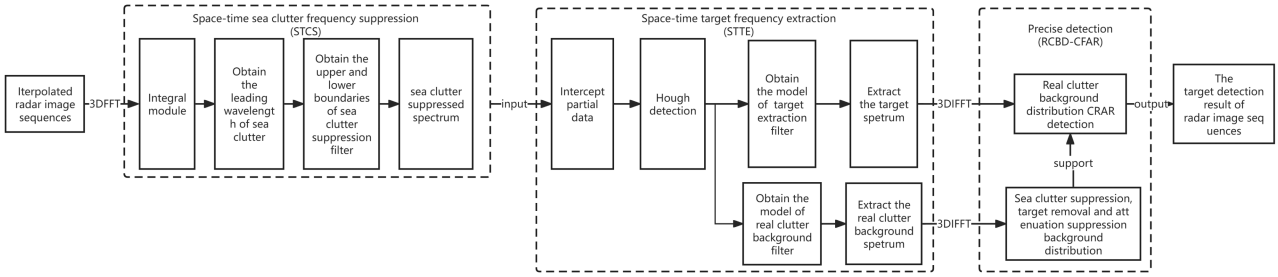

Fig. 8. Detailed stepwise structure of the STCS, STTE, and RCBD–CFAR segments.

TABLE I
X-BAND MARINE RADAR PARAMETERS

Radar parameters	Performance
Electromagnetic wave frequency	9.4 GHz
Antenna angular speed	26 r/min
Antenna height	25 m
Polarization	HH
Range resolution	7.5 m
Horizontal beam width	1.3°
Vertical beam width	23°
Pulse repetition Frequency	1300 Hz
Pulsewidth	0.7°

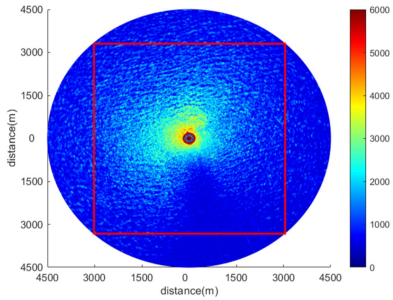

Fig. 9. Interpolation area (delineated by the red-edged square) in the original radar image.

threshold, it is classified as background clutter point and denoted as H_0.

Fig. 8 is a block diagram of the STCS, STTE, and RCBD-CFAR stages. The content proposed in this article is STTE and RCBD-CFAR. During the STTE process, a target extraction model and a background clutter extraction model are established by using Hough detection. The sea clutter suppression, target removal and attenuation suppression clutter background distribution is employed to determine the CFAR detection threshold for precise detection in the RCBD-CFAR process.

IV. EXPERIMENTAL RESULTS

This section evaluates the performance of the proposed marine radar target detection algorithm on authentic radar image sequences and moving targets. After presenting the radar parameters and employed data, it provides the experimental results on band marine radar data. Finally, it compares the performance of the proposed target detection method with those of excellent algorithms.

A. Marine Radar Parameters and Experimental Data

The data were collected from the China East Sea in October of 2017 using an X-band marine radar and included both target and sea clutter signals. Table I presents the radar parameters of the experiment. Each image captured by the radar contains 2048 lines, and each line comprises 600 range bins.

Nearest neighbor interpolation is employed for converting the square region from polar coordinates to Cartesian coordinates. Interpolation converts Point $A(r, \theta, z)$ in polar coordinates to its corresponding coordinates $A^d(x, y, z)$ in Cartesian coordinates. The proposed method is applied to a scale of $848 \times 848 \times 32$ pixels image sequence, as shown in Fig. 9.

One set of image sequences comprises 32 consecutive images collected over a period of approximately 80 s, encompassing moving targets with their speed and direction information embedded within the sequence. The position and intensity of the target constantly change with each captured image.

The dataset in the experiment exhibits a significant wave height (height of highest one-third wave) ranging from 1.5 to 3.5 m. This range was categorized into three distinct sea conditions: low sea condition (1.5 m$\sim$2.2 m), medium sea condition (2.2 m$\sim$2.9 m), and high sea condition (2.9 m$\sim$3.5 m).

Ten real moving target continuous signal datasets with different sizes (25$\sim$200 pixels), velocities (10$\sim$20 m/s), directions (0°$\sim$ 360°), trajectories, and initial grayscale value variations (0$\sim$3560) were extracted from the actual radar image sequence data. Fig. 10(a)–(c) shows three types of moving target continuous signals extracted from the real images sequence. Fig. 11 depicts multiple motion trajectories of selected moving targets in the real image sequences. The trajectories are nearly uniform and linear within a set of sequences.

To further evaluate the performance of the proposed algorithm, the grayscale values of the extracted real target space–time signals were adjusted using the α coefficient to simulate different radar cross-section (RCS) scenarios. Fig. 10(d)–(f) illustrates the processing results of the aforementioned three targets with $\alpha = 1.2$. The grayscale values of the real target space–time signals were globally reduced without affecting the size or other conditions. In addition to the target information,

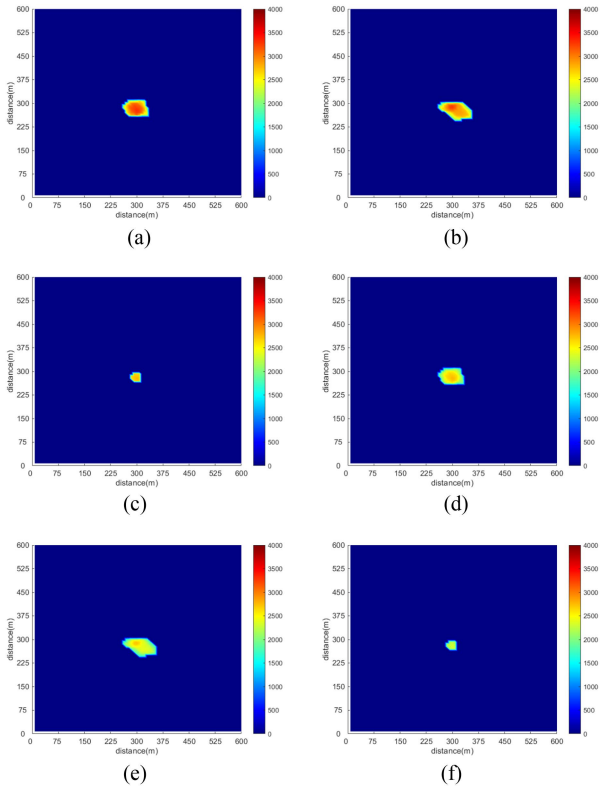

Fig. 10. Three real moving target continuous signals and their corresponding target continuous signals adjusted with α. (a) First target. (b) Second target. (c) Third target. (d) First target ($\alpha = 1.2$). (e) Second target ($\alpha = 1.2$). (f) Third target ($\alpha = 1.2$).

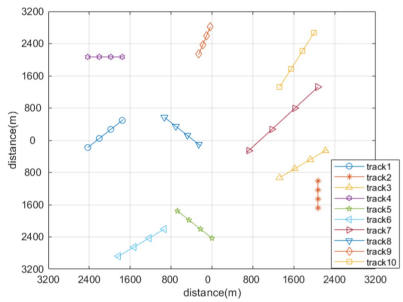

Fig. 11. Movement trajectories of real targets extracted from experimental data.

the single-image sequences of sea clutter from different marine environment data were extracted. To obtain image-sequence data under various RCS scenarios, target space–time sequences with different RCS values were combined with pure sea clutter sequences. During the addition process, the grayscale values of the target edge points were adjusted based on the sea clutter grayscale values near the target. Fig. 12(a)–(c) shows images of the different RCS targets under low, medium, and high sea conditions, respectively, with multiple targets enclosed within red bounding boxes. To mitigate the echo saturation caused by strong radar echoes in the central region, a portion of the central data was removed through data reduction.

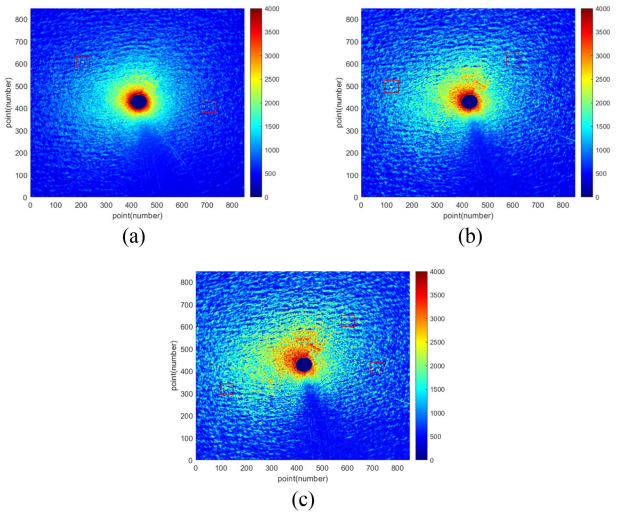

Fig. 12. Radar images of different RCSs under different sea conditions.

B. Performance of Target Detection Under Real Radar Data

Fig. 13 shows the algorithm processing results under the low, medium, and high sea conditions. Shown are the original images, frequency spectra of the original images in the $V_{\omega,k}$ domain, frequency spectra of sea-clutter suppression in the $V_{\omega,k}$ domain, target extraction spectra in the wavenumber domain, and the final processed images. The original images contain the same three targets under all three conditions. The first target, located in the lower left corner of the image, comprises 36 pixels with an average grayscale value of 2492 and moves northeast at 20 m/s. The second target, located in the upper right of the image, consists of 28 pixels with an average grayscale value of 2350 and moves northward at 15 m/s. The third target, located in the right part of the image, is composed of 44 pixels with an average grayscale value of 2332 and progresses westward at 10 m/s. The sea conditions depicted in Fig. 13(a) and (f), and correspond to sea heights of 1.98, 2.55, and 3.11 m, respectively, with corresponding average sea-clutter intensities of 1789, 2298, and 2673, respectively. The energies of the sea spikes within the whole image increased with increasing sea state. The target is easily submerged by sea clutter in moderate to high sea states. The spectral energy of the sea clutter [see Fig. 13(b), (g), and (i)] also gradually increased with increasing sea state. Furthermore, as the sea states intensified, the scattering of electromagnetic waves by the sea surface became increasingly complicated, producing stronger background noise in the images. The $V_{\omega,k}$ domain spectra [see Fig. 13(c), (h), and (m)] were obtained by selectively filtering out the sea clutter frequencies during the sea clutter suppression stage. Although the dominant frequencies of sea clutter were eliminated from the spectrum, the energy of the moving targets in the frequency domain was drowned by the substantial quantity and high intensity of residual energy from other noises in the entire image, and remained difficult to detect. However, the target energy was readily detected in the wavenumber domain. The target frequencies in the wavenumber domain, are depicted in Fig. 13(d), (i), and (n). The dominant

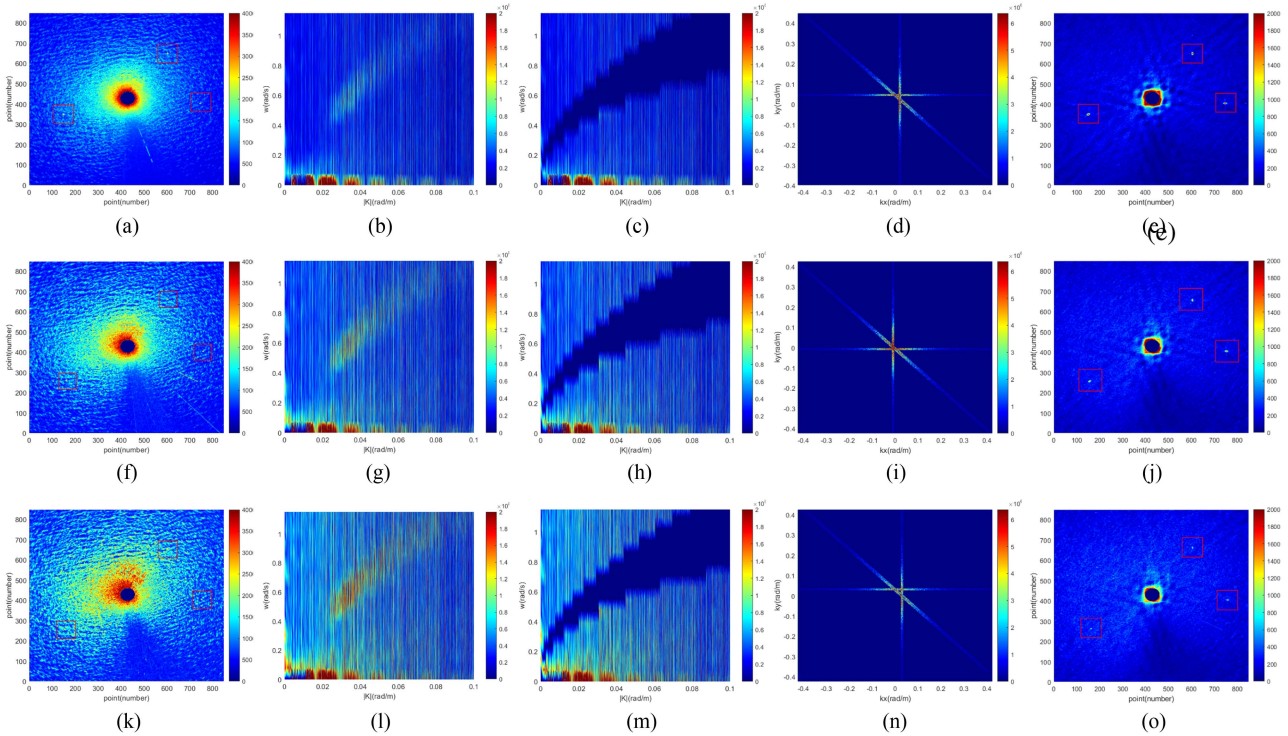

Fig. 13. Results of the treatment process of the proposed method under different SCR conditions (first line: low sea state, second line: medium sea state, and third line: high sea state). (a), (f), and (k) 16th original images in the sequences. (b), (g), and (l) Frequency spectra of the original images in the $V_{\omega,k}$ domain. (c), (h), and (m) 16th 2-D cross-sectional frequency spectra of sea clutter suppression in the $V_{\omega,k}$ domain. (d), (i), and (n) Target-extraction spectra in the wavenumber domain. (e), (j), and (o) 16th final processed images in the sequences.

target frequencies in the low, moderate, and high sea states were effectively identified and extracted from the 16th, 18th, and 20th wavenumber spectra, respectively. As shown in Fig. 13(e), (j), and (o), the sea clutter was efficiently suppressed and the targets were successfully extracted under varying sea conditions. A minimal portion of an intense signal persisted in the central region of the image, resulting from incomplete removal of the central saturation region in the space–time domain. Although some clutter was retained, its average energy was too low to be treated as sea spikes, thus avoiding potential interference with the subsequent precise detection process.

Because of the lack of Doppler information and the ability to accumulate signals for an extended period, noncoherent scanning marine radar exhibits suboptimal performance in processing echo data across the temporal domain, frequency domain, and time—frequency domain. The effectiveness of sea clutter suppression in the 3-D frequency–wavenumber domain substantiates the stability of sea clutter background characteristics in the space–time domain. Moreover, this approach obviates reliance on phase information while achieving effective sea clutter suppression and target detection solely based on amplitude information, rendering it suitable for fast scanning noncoherent marine radar [31]. The method in this manuscript is based on an improvement of this method. The SVD-FRFT is widely employed for sea clutter suppression in marine radars and has been validated in [37] and [38]. Despite its diminished efficacy when applied to our radar, it still exhibits a favorable effect. Therefore, to assess the performance of the proposed method in sea-clutter suppression, the performance measures for the comparative experiment were the individual STCS and SVD-FRFT.

SCR improvement was calculated as follows:

$$\mathrm{SCR}_r = 20\log\left(\frac{\langle s_p(n)\rangle}{\langle x_p(n)\rangle}\right) - 20\log\left(\frac{\langle s_0(n)\rangle}{\langle x_0(n)\rangle}\right) \tag{23}$$

where s_p and s_0 represent the sums of the grayscale values of all target points in the output and original images, respectively, x_p and x_o represent the sums of the grayscale values of all background clutter in the output and original images, respectively, and $<>$ denotes the averaging of these sums.

Fig. 14 shows the processing results using the aforementioned three algorithms under the low, moderate, and high sea conditions. Table II presents the SCR_r realized by the three methods on four different original SCRs covering low, moderate, and high sea states. With the proposed method, the SCR was consistently improved by approximately 17 dB under low sea conditions and at least 14 dB under moderate sea conditions. In high sea states, the SCR_r are 10.7 and 12.8 dB on original SCRs with 0.8 and 3.9 dB, respectively. As the sea condition intensified, the intensity of the generated background noise increased and more noise spectral energy was extracted throughout the wavenumber domain during the target-frequency extraction. The SCR enhancement decreased accordingly. Furthermore, when the target grayscale value was weakened to a level comparable to that of sea clutter, the frequency spectra of the sea clutter points were convoluted with those of the target edge points,

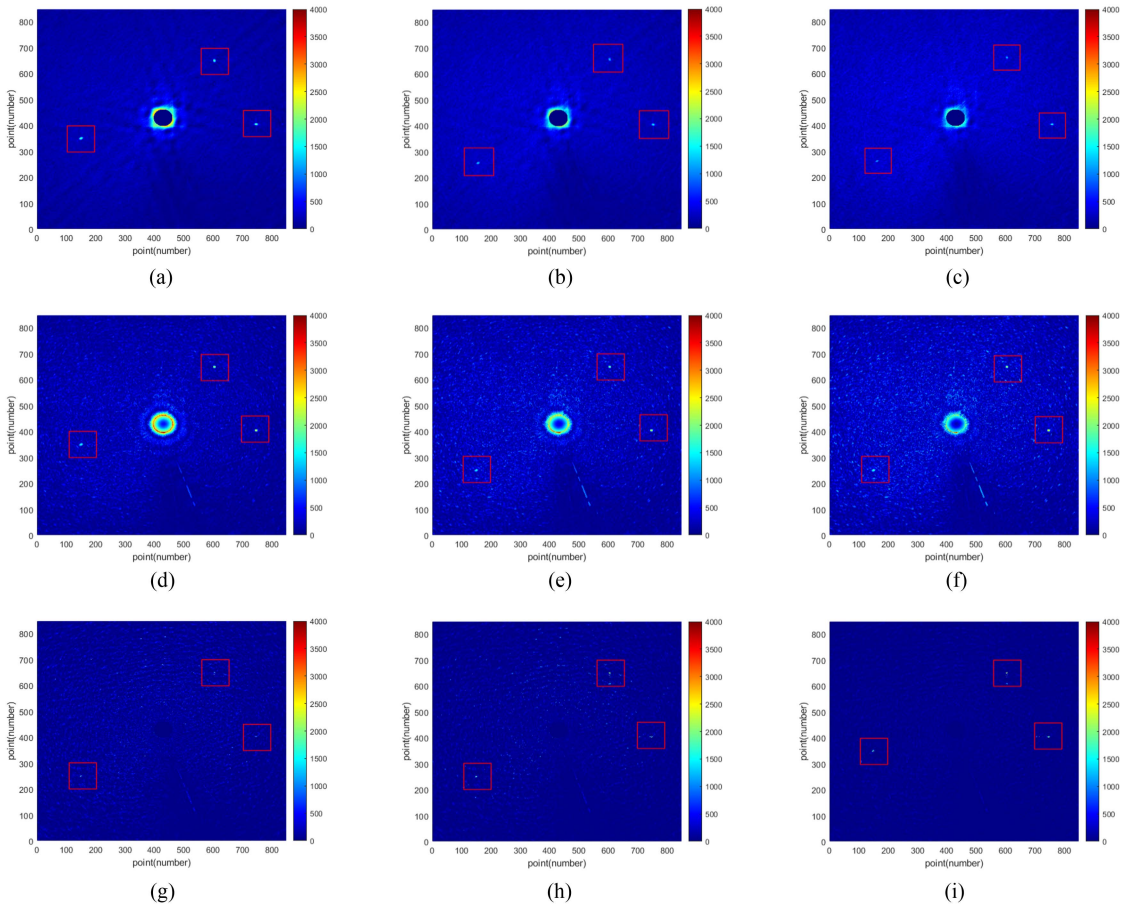

Fig. 14. Results of three methods under different sea states (first column: low sea state, second column: medium sea state, and third column: high sea state). (a)–(c) 16th final processed images in the sequence by using the proposed method. (d)–(f) 16th final processed images in the sequence by using individual STCS. (g)–(i) 16th final processed images in the sequence by using SVD-FRFT.

TABLE II
SCR IMPROVEMENT RESULTS USING INDIVIDUAL STCS, SCD-FRFT, AND PROPOSED METHOD

		Low sea state			Moderate sea state			High sea state		
	Method	Original image	Extracted image	SCRr	Original image	Extracted image	SCRr	Original image	Extracted image	SCRr
SCR1(dB)	Proposed method	3.60	20.80	17.20	2.10	16.30	14.20	0.80	11.50	10.70
	Individual STCS		12.72	9.12		9.94	7.84		9.32	8.52
	SVD-FRFT		10.92	7.32		5.58	3.48		2.19	1.39
SCR2(dB)	Proposed method	4.70	22.00	17.30	3.30	17.70	14.40	2.00	14.20	12.20
	Individual STCS		14.44	9.74		12.34	9.04		11.48	9.48
	SVD-FRFT		12.73	8.03		7.88	4.58		6.08	4.08
SCR3(dB)	Proposed method	5.70	23.00	17.30	4.30	18.70	14.40	3.00	15.40	12.40
	Individual STCS		16.56	10.86		14.34	10.04		12.96	9.96
	SVD-FRFT		14.03	8.33		9.96	5.66		7.64	4.64
SCR4(dB)	Proposed method	w6.70	24.00	17.30	5.20	19.90	14.70	3.90	16.70	12.80
	Individual STCS		18.05	11.35		16.11	10.91		14.56	10.66
	SVD-FRFT		14.60	7.90		11.34	6.14		9.61	5.71

causing leakage of target-point information when filtering out the sea clutter for target extraction. When the SCR reaches a certain threshold, the energy of the extracted targets reduces because target points are lost, slightly degrading the efficacy of SCR enhancement. The threshold increases as the sea clutter intensifies under different sea conditions. In individual STCS, the SCR was improved by at least 9.12 dB under low sea conditions and by 7.84 dB under moderate sea conditions. In high sea states, the SCR enhancement was improved at least by 8.52 dB from the original SCR of 0.8 dB. Under the same states, individual STCS exhibited some reduction compared to the proposed method. This reduction can be attributed to the fact that the spectrum obtained through the individual STCS method includes not only energy from targets but also static and quasistatic energy, the characteristic frequency of nonlinear waves, the high-order harmonic frequency, the aliased spectrum, and background noise. The SCR improvement range of the SVD-FRFT method was between 1.39 and 8.33 dB. The performance

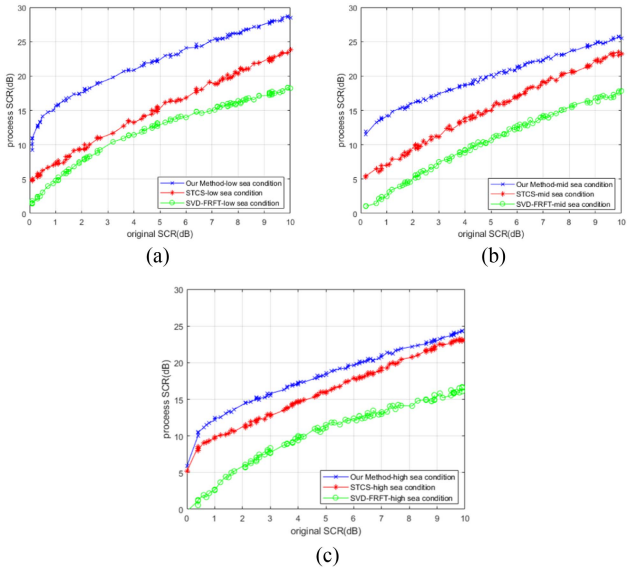

Fig. 15. Comparison of SCR improvement effects under (a) low sea condition, (b) mid sea condition, and (c) high sea condition.

of SVD-FRFT was affected by the low sampling frequency of incoherent scanning marine radar, which lowered its ability to retain rapidly moving targets. The ability of SVD-FRFT to suppress sea clutter was better than that of individual STCS, which was similar to that of the proposed method, as shown in Fig. 14(g), (h), and (i), however it excessively suppressed target energy, mistakenly treating a portion of the target point as sea clutter, which accounted for the limited SCR_r achieved.

Next, combining real radar-image data of low, moderate, and high sea states with multiple targets and setting distinct α coefficients, 300 experimental samples were generated for further evaluation of three methods. To ensure coverage across the 0–10 dB range of SCRs, 100 sets of samples were collected for each sea state. As shown in Fig. 15, the proposed method performed optimally under low sea conditions, registering a superior improvement of 18.5 dB at maximum. Under moderate and high sea conditions, the peak improvements were 15.8 and 14.4 dB, respectively. The proposed method demonstrated a substantial improvement in SCR_r compared to the individual STCS method, with a maximum difference value of up to 9.01 dB and an average difference value of approximately 6.76 dB under low sea states. In comparison to the SCRr of the SVD-FRFT method, the maximum difference value reached 11.06 dB, with an average difference value of 9.99 dB. Under medium sea conditions, the proposed exhibited a maximum difference value of 7.62 dB and an average difference value of around 4.74 dB compared to the individual STCS method, and it exhibited a maximum difference value of 11.80 dB and an average difference value of around 9.41 dB compared to the SVD-FRFT method. Under high sea conditions, the proposed method achieved a maximum difference value of 3.39 dB and an average difference value of approximately 2.05 dB in SCR_r compared to the individual STCS method. Meanwhile, it exhibited a maximum difference value of 10.03 dB and an average difference value of approximately 7.89 dB in SCR_r compared to the SVD-FRFT method.

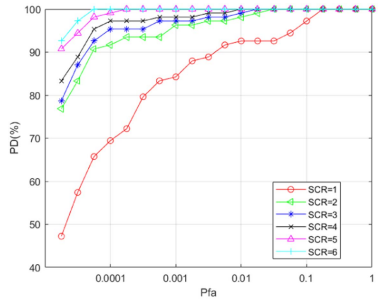

Fig. 16. ROC curves under typical SCR conditions.

As the sea clutter intensified under different sea conditions, the performance of the proposed method and the SVD-FRFT method worsened. Conversely, the performance of the individual STCS method improved. The experimental results demonstrate that the proposed approach effectively suppresses sea clutter and extracts targets under varying sea conditions, considerably enhancing the SCR of the output image for subsequent target detection processes. The performance is superior to the other two methods.

C. Comparison of Detection Performance

Next, binary detection was performed on ACCS-CFAR-processed images. The detection performance was evaluated in terms of two indices: the probability of detection and the false alarm rate, respectively, calculated as

$$P_D = \frac{N_m dt}{N_t} \tag{24}$$

$$P_{\mathrm{fa}} = \frac{N_{fa}}{N_t} \tag{25}$$

where N_t and N_{dt} represent the total numbers of all target points and detected target points, respectively, and N_{fa} represents the total number of detected nontarget points.

The receiver operating characteristic (ROC) curves under typical SCR conditions are displayed in Fig. 16. Under equivalent P_{fa} conditions, an increasing trend in P_D is manifested with respect to the increase in SCR. However, a significant decline in detection performance is experienced when the SCR is about 1 dB. This deterioration can be attributed to suppression of the target edges when filtering out the sea clutter. When P_{fa} exceeds 0.0001 and the SCR exceeds 2 dB, the P_D can exceed 90%. At this time, the P_D approached with a P_{fa} of 0.001.

The performance measures for the comparative experiment were the classical CA-CFAR and the weighted likelihood CFAR (WL-CFAR, Weibull condition) [39], which estimates the scale parameters of the Weibull distribution using the maximum-weighted logarithmic likelihood function. Given a preset P_{fa}, the WLCFAR adaptively determines the threshold, enabling target detection. The shape parameter C, sliding-window scale N, robustness measurement parameter β, and of τ of the WL-CFAR detector were set to 1.2, 16, 0.1, and 0.0001, respectively. The sliding window N and P_{fa} of the classic CA-CFAR detector were set to 16 and 0.0001, respectively. The P_{fa} of the ACCS–CFAR

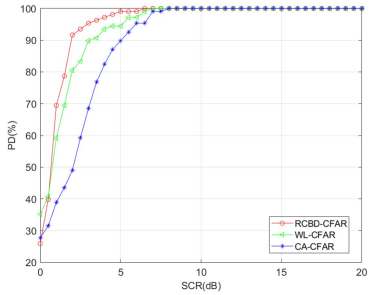

Fig. 17. Comparison of detection performances of different methods on a test set of radar images processed using the proposed methods.

detector was set to 0.0001. Fig. 17 compares the detection performances of different methods on a test set of radar images after processing with the proposed methods. The conventional CA-CFAR detector obtained good detection results at high SCR but its performance notably declined as the SCR decreased. In contrast, the WL-CFAR and ACCS–CFAR detectors achieved outstanding detection performance on all processed images. Although the ACCS–CFAR detector was slightly inferior to the other two detectors near, it outperformed its competitors in other SCR ranges because it incorporates the real background distribution. The classic CA-CFAR detector lacked robustness, as evidenced by a noteworthy number of false alarms in the presence of intricate and fluctuating background clutter. In contrast, the WL-CAR detector effectively detected the target points but produced more false alarms than the proposed ACCS-CFAR.

To assess the efficacy of marine radar target detection based on spatiotemporal domain joint filtering in complex sea clutter environments, several methods applicable to marine radar, namely, WHOS-CFAR, GMOS-CFAR, SVD-FRFT-CFAR, and STCS-CFAR, were compared. WHOS-CFAR and GMOS-CFAR have been validated to provide superior detection performance under Pareto distribution and Weibull distribution in [35], [40], and [41], respectively. By establishing detectors that follow WHOS or GMOS decision rules, the methods achieve full CFAR characteristics while avoiding parameter estimation of the distribution model. The WHOS-CFAR and GMOS-CFAR are the spatial domain methods and are suitable for noncoherent fast scanning marine surveillance radar. In addition, SVD-FRFT and STCS, as advanced sea clutter suppression and target detection methods in the frequency and spatiotemporal domains, respectively, were used for comparison.

Fig. 18 displays the truth images, STFTD (the proposed method) detection images, individual STCS-CFAR detection images, SVD-FRFT-CFAR detection images, GMOS-CFAR detection images, and WHOS-CFAR detection images under the low, moderate, and high sea conditions. The target of 36 pixels is selected and integrated into three different positions to obtain different SCR data. The targets are enclosed within red rectangular boxes and amplified by an amplifier for a clearer display. The grayscale values within the image are segregated into three distinct categories. The points with a grayscale value of 3 (marked in red) are designated as the correctly detected target points. The points with a grayscale value of 2 (depicted in orange) indicate the erroneously detected target points. The points with a grayscale value of 1 (depicted in green) indicate target points that were not detected.

TABLE III
DETECTION PROBABILITIES OF DIFFERENT METHODS UNDER DIFFERENT SEA CONDITIONS

	Low sea state	Moderate sea state	High sea state
Proposed method PD	99.89%	95.34%	94.44%
GMOS-CFAR PD	90.74%	85.19%	83.33%
WHOS-CFAR PD	84.33%	79.63%	75.93%
STCS-CFAR PD	97.22%	94.44%	90.74%
SVD-CFAR PD	82.41%	51.85%	17.59%

P_{fa} was set to 0.0001, and the detection results of all methods are shown in Table III. The P_D of the proposed method in three sea conditions reaching 94.44%, 95.34%, and 99.89%, respectively, which were the highest among all methods. Because of the high-intensity points retained after suppression and extraction processing mainly surrounding the target points, the false alarm points were mainly concentrated at the edge of the targets. The P_D of individual STCS-CFAR was the second highest, reaching 90.74%, 94.44%, and 97.22%, respectively. The small portion high-intensity noise points presented in the suppressed image formed most of the false alarm points in this detection result. The detection performance of the GMOS-CFAR method decreased compared to the individual STCS-CFAR method, reaching 83.33%, 85.19%, and 90.74% in the three sea conditions, respectively. The false alarm points were concentrated around the targets. The P_D of the WHOS-CFAR method under the three sea conditions were 75.93%, 79.63%, and 84.33%, respectively, slightly lower than the GMOS-CFAR method. The reason is that the sea clutter distribution model of marine surveillance radar with high resolution and low grazing angle is closer to the Weibull distribution compared to the Pareto distribution. The P_D of the SVD-FRFT-CFAR method were 17.59%, 51.85%, and 82.41%, respectively. Due to the loss of target energy during the sea clutter suppression, the P_D sharply decreased in medium to high sea conditions.

The SCR-PD curves of the five methods, with P_{fa} set at 0.0001, are compared in Fig. 19. The P_D of the proposed method exceed 90% at around 2 dB and reached 100% at around 6.5 dB. STCS-CFAR, GMOS-CFAR, WHOS-CFAR, and SVD-FRFT-CFAR achieved 100% detection probability around 7, 8, 10.5, and 11.5 dB, respectively. The detection probability of the proposed method increased by an average of 11.2% compared to the STCS method, 17.95% compared to GMOS-CFAR, 23.79% compared to WHOS-CFAR, and 55.94% compared to SVD.

V. DISCUSSION

Previous studies focused on suppressing sea clutter energy, resulting in a spectrum that not only contains target energy but also includes other noise energy [31]. Building upon this foundation, in this study, a model for target energy in the frequency–wavenumber domain was established, and an effective strategy for extracting target energy was proposed. As a result of this step, the aforementioned nontarget energy could be significantly suppressed in the obtained spectrum. Compared to individual STSC and SVD-FRFT methods, the proposed approach improves the

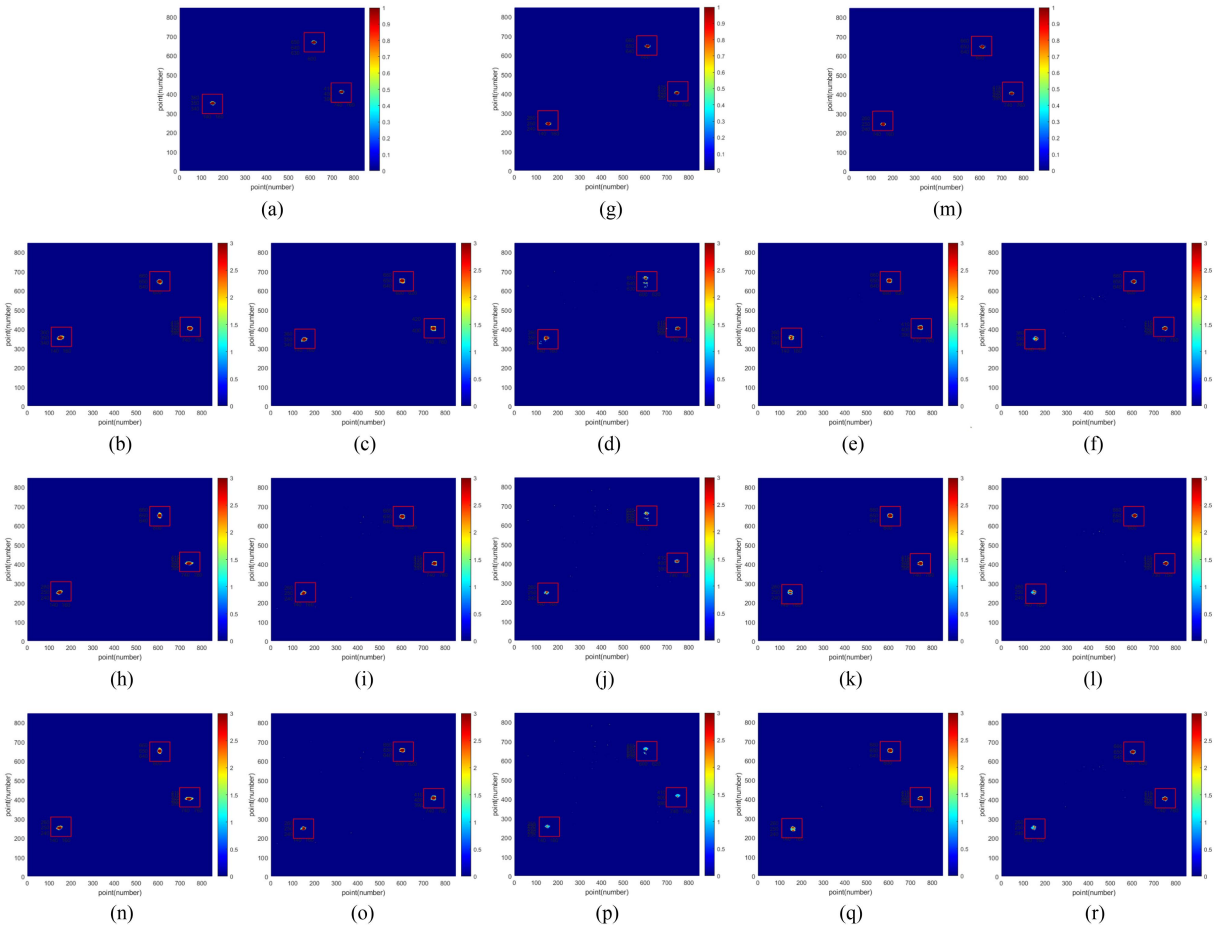

Fig. 18. Results of target detection by different methods under different sea conditions [(b)–(f) Low sea state, (h)–(l) medium sea state, and (n)–(r) high sea state]. (a), (g), and (m) 16th truth images in the sequence. (b), (h), and (n) 16th proposed method detection images in the sequence. (c), (i), and (o) 16th individual STCS-CFAR detection images in the sequence. (d), (j), and (p) 16th SVD-FRFT-CFAR detection images in the sequence. (e), (k), and (q) 16th GMOS-CFAR detection images in the sequence. (f), (l), and (r) 16th WHOS-CFAR detection images in the sequence.

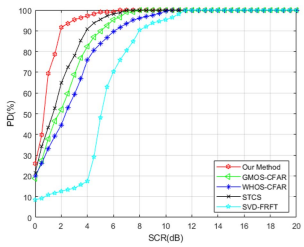

Fig. 19. Comparison of detection performances of different methods.

SNR by an average of 6.76 and 9.99 dB, respectively, thereby enhancing image quality under complex sea conditions and low SCR conditions. Furthermore, previous articles have explored various spatial domain incoherent CFAR detection methods [7], [8], [35], [39], [40], [41]. However, traditional CFAR detection performance has been found to be unstable when dealing with complex variations in real sea clutter backgrounds. Our study demonstrates that by excluding sea clutter and targets from real-time background clutter analysis while avoiding fitting operations and the normalization factor τ. The proposed method can maintain CFAR ability and stability even under complex and changing real sea clutter backgrounds while improving detection probability. The proposed method outperforms the traditional CFAR techniques such as GMOS-CFAR and WHOS-CFAR by at least 11.2%.

Although the proposed method showed effective results, there are still some avenues for future research and improvement. First, in the filtering method set $\omega \in [K_n, K_p]$ to enhance the clarity of the energy spectrum for the subsequent target-extraction procedures. However, this approach caused a slight loss of target energy during the extraction process. Consequently, the grayscale value of the target in the spatiotemporal domain image decreased, indirectly suppressing the enhancement of the SCR in the processed image. Second, unlike other methods that solely utilize time domain (frequency domain) or space domain, this approach integrates both space and time domains (image sequence) to capture more comprehensive information. However, a drawback is that it requires substantial time to accumulate images, with a set of image sequences taking approximately 80 s. This makes it slower compared to other target detection methods and unable to provide immediate results. Third, although the target data used in this article is extracted from real radar images and the gray value is adjusted accordingly to achieve weak target (low SCR) detection performance, the size of the target remains unaltered. The targets are generally

150-m long, with the smallest length being more than 50 m, falling into the medium to large category rather than miniature. For microtargets, the performance of the proposed algorithm will be significantly reduced. Fourth, in scenarios where the target exhibits uniform linear motion, its spectral lines maintain consistent slopes at the wavenumber domain corresponding to each discrete frequency ω while exhibiting identical spacing between the wavenumber plane of adjacent ω. For a target moving in a variable direction, the velocity direction continues to change, leading to corresponding changes in the values of v_{ix}/v_{iy} and resulting in a constant change in the slope of the spectral lines at the wavenumber domain corresponding to each discrete frequency ω. Consequently, the target spectrum will manifest as a series of lines with varying slopes but consistent spacing. The changing trend of the slope is consistent with the trend of the target direction changing. In cases of targets exhibiting variable velocity motion, ω_i/v_{iy} undergo continuous changes, leading to different spacing between spectral lines in wavenumber domains corresponding to adjacent discrete frequencies ω. As a result, the final target spectrum appears as a series of lines with uniform slope but varying spacing, this spacing changing trend aligns with variations in target velocity. In the detection of variable speed and small variable direction targets, increasing the value of the spread width coefficient C_i can ensure the extraction ability of target frequency and well applicability. However, for targets with high moving directional change, a large C_i is required, which may reduce sea clutter suppression effect and impact the detection performance of the proposed method. Future research will focus on exploring more sophisticated filtering processes, including adjustments to the boundaries in both the θ dimension and ω dimension, to ensure the maximum retention of target energy. Second, the selection of the width expansion coefficient of the target model will affect the extraction effect of target energy. The relationship between it and the real target needs to be further studied in order to obtain the target energy more accurately and completely.

VI. Conclusion

This study proposed and evaluated a STAF algorithm based on the Hough transform algorithm, which detects targets in sequences of marine radar images. The method adopts a two-stage approach: coarse detection followed by precise detection. The coarse detection phase filters out the complex and variable spatiotemporal sea clutter, effectively suppressing the sea spikes and other clutter energies that interfere with target detection. The precise detection phase utilizes the real-time background clutter through sea-clutter suppression and target removal, enabling rapid and accurate detection on the images processed in the previous phase. Experimental results obtained from massive real marine radar images demonstrated that the proposed method outperforms other detection methods, especially under complex, variable, and heavy sea clutter conditions. Moreover, the proposed approach simultaneously achieves excellent detection rates and produces few false alarms.

References

[1] L. Sun, Z. Lu, Y. Wei, and H. Wang, "A new method to retrieve rainfall intensity level from rain-contaminated X-band marine radar image," *Int. J. Remote Sens.*, vol. 44, no. 2, pp. 585–608, 2023.

[2] X. Chen, W. Huang, and M. C. Haller, "A novel scheme for extracting sea surface wind information from rain-contaminated X-band marine radar images," *IEEE J. Sel. Topics Appl. Earth Observ. Remote Sens.*, vol. 14, pp. 5220–5234, May 2021.

[3] B. Lund, H. C. Graber, and R. Romeiser, "Wind retrieval from shipborne nautical X-band radar data," *IEEE Trans. Geosci. Remote Sens.*, vol. 50, no. 10, pp. 3800–3811, Oct. 2012.

[4] Y. Wei, Y. Liu, Y. Lei, R. Lian, Z. Lu, and L. Sun, "A new method of rainfall detection from the collected X-band marine radar images," *Remote Sens.*, vol. 14, no. 15, 2022, Art. no. 3600.

[5] J. Pei et al., "A sea clutter suppression method based on machine learning approach for marine surveillance radar," *IEEE J. Sel. Topics Appl. Earth Observ. Remote Sens.*, vol. 15, pp. 3120–3130, Apr. 2022.

[6] S. Chen, C. Feng, Y. Huang, X. Chen, and F. Li, "Small target detection in X-band sea clutter using the visibility graph," *IEEE Trans. Geosci. Remote Sens.*, vol. 60, Jun. 2022, Art. no. 5115011.

[7] P. Huang, Z. Zou, X.-G. Xia, X. Liu, and G. Liao, "A statistical model based on modified generalized-k distribution for sea clutter," *IEEE Geosci. Remote Sens. Lett.*, vol. 19, Jul. 2022, Art. no. 8015805.

[8] J. Xue, J. Liu, S. Xu, and M. Pan, "Adaptive detection of radar targets in heavy-tailed sea clutter with lognormal texture," *IEEE Trans. Geosci. Remote Sens.*, vol. 60, Dec. 2022, Art. no. 5108411.

[9] Y. Fan, M. Tao, and J. Su, "Multifractal correlation analysis of autoregressive spectrum-based feature learning for target detection within sea clutter," *IEEE Trans. Geosci. Remote Sens.*, vol. 60, Dec. 2022, Art. no. 5108811.

[10] M.-J. Lee, S.-J. Lee, B.-H. Ryu, B.-G. Lim, and K.-T. Kim, "Reduction of false alarm rate in SAR-MTI based on weighted kurtosis," *IEEE Trans. Geosci. Remote Sens.*, vol. 59, no. 4, pp. 3122–3135, Apr. 2021.

[11] H. Wang and L. Cai, "A localized adaptive MTD processor," *IEEE Trans. Aerosp. Electron. Syst.*, vol. 27, no. 3, pp. 532–539, May 1991.

[12] Y. Yang, S.-P. Xiao, and X.-S. Wang, "Radar detection of small target in sea clutter using orthogonal projection," *IEEE Geosci. Remote Sens. Lett.*, vol. 16, no. 3, pp. 382–386, Mar. 2019.

[13] J. Cai, H. Zhou, W. Huang, and B. Wen, "Ship detection and direction finding based on time-frequency analysis for compact HF radar," *IEEE Geosci. Remote Sens. Lett.*, vol. 18, no. 1, pp. 72–76, Jan. 2021.

[14] J. Xiang, X. Lv, X. Fu, and Y. Yun, "Detection and estimation algorithm for marine target with micromotion based on adaptive sparse modified-LV's transform," *IEEE Trans. Geosci. Remote Sens.*, vol. 60, Dec. 2022, Art. no. 5108617.

[15] X. Chen, X. Yu, J. Guan, and J. Zhang, "Detection and extraction of marine target with micromotion via short-time fractional Fourier transform in sparse domain," in *Proc. IEEE Int. Conf. Signal Process. Commun. Comput.*, 2016, pp. 1–5.

[16] X. Yu, X. Chen, Y. Huang, and J. Guan, "Fast detection method for low-observable maneuvering target via robust sparse fractional Fourier transform," *IEEE Geosci. Remote Sens. Lett.*, vol. 17, no. 6, pp. 978–982, Jun. 2020.

[17] H. Zhang, T. Shan, S. Liu, and R. Tao, "Performance evaluation and parameter optimization of sparse Fourier transform," *Signal Process.*, vol. 179, 2021, Art. no. 107823.

[18] X. Chen, X. Mu, J. Guan, N. Liu, and W. Zhou, "Marine target detection based on marine-faster r-CNN for navigation radar plane position indicator images," *Front. Inf. Technol. Electron. Eng.*, vol. 23, no. 4, pp. 630–643, 2022.

[19] X. Mou, X. Chen, J. Guan, Y. Dong, and N. Liu, "Sea clutter suppression for radar PPI images based on SCS-GAN," *IEEE Geosci. Remote Sens. Lett.*, vol. 18, no. 11, pp. 1886–1890, Nov. 2021.

[20] X. Chen, J. Guan, X. Mu, Z. Wang, N. Liu, and G. Wang, "Multi-dimensional automatic detection of scanning radar images of marine targets based on radar PPINet," *Remote Sens.*, vol. 13, no. 19, 2021, Art. no. 3856.

[21] L. Wen, J. Ding, and Z. Xu, "Multiframe detection of sea-surface small target using deep convolutional neural network," *IEEE Trans. Geosci. Remote Sens.*, vol. 60, Oct. 2022, Art. no. 5107116.

[22] Y. Xia, N. Zhang, H. Kuang, and Y. Zhang, "Detection & tracking method for radar target based on plot-track quality evaluation," *J. Eng.*, vol. 2019, no. 19, pp. 6239–6243, 2019.

[23] Y. Zhou, H. Su, S. Tian, X. Liu, and J. Suo, "Multiple-kernelized-correlation-filter-based track-before-detect algorithm for tracking weak and extended target in marine radar systems," *IEEE Trans. Aerosp. Electron. Syst.*, vol. 58, no. 4, pp. 3411–3426, Aug. 2022.
[24] X. Chen, J. Guan, Y. Huang, N. Liu, and Y. He, "Radon-linear canonical ambiguity function-based detection and estimation method for marine target with micromotion," *IEEE Trans. Geosci. Remote Sens.*, vol. 53, no. 4, pp. 2225–2240, Apr. 2015.
[25] X. Chen, J. Guan, N. Liu, and Y. He, "Maneuvering target detection via radon-fractional Fourier transform-based long-time coherent integration," *IEEE Trans. Signal Process.*, vol. 62, no. 4, pp. 939–953, Feb. 2014.
[26] G. Zhou, L. Wang, and T. Kirubarajan, "A pseudo-spectrum approach for weak target detection and tracking," *IEEE Trans. Aerosp. Electron. Syst.*, vol. 55, no. 6, pp. 3394–3412, Dec. 2019.
[27] S. Chen and W. Huang, "Maneuvering target tracking from nautical radar images using particle-Kalman filters," *J. Electromagn. Waves Appl.*, vol. 27, no. 18, pp. 2366–2378, 2013.
[28] H. Zhang, Y. Liu, Y. Ji, and L. Wang, "Vessel fusion tracking with a dual-frequency high-frequency surface wave radar and calibrated by an automatic identification system," *Acta Oceanologica Sinica*, vol. 37, no. 7, pp. 131–140, 2018.
[29] B. Yan, L. Xu, M. Li, and J. Z. Yan, "Track-before-detect algorithm based on dynamic programming for multi-extended-targets detection," *IET Signal Process.*, vol. 11, no. 6, pp. 674–686, 2017.
[30] B. Errasti-Alcala, W. Fuscaldo, P. Braca, and G. Vivone, "Realistic extended target model for track before detect in maritime surveillance," in *Proc. OCEANS*, 2015, pp. 1–9.
[31] B. Wen, Y. Wei, and Z. Lu, "Sea clutter suppression and target detection algorithm of marine radar image sequence based on spatio-temporal domain joint filtering," *Entropy*, vol. 24, no. 2, 2022, Art. no. 250.
[32] K. Reichert, K. Hessner, J. Dannenberg, and I. Trankmann, "X-band radar as a tool to determine spectral and single wave properties," in *Proc. Int. Conf. Offshore Mechanics Arctic Eng.*, 2006, vol. 47489, pp. 683–688.
[33] J. C. Nieto-Borge, P. Jarabo-Amores, D. de la Mata-Moya, and K. Hessner, "Signal-to-noise ratio analysis to estimate ocean wave heights from x-band marine radar image time series," *IET Radar, Sonar Navig.*, vol. 2, no. 1, pp. 35–41, 2008.
[34] X. Liu, W. Huang, and E. W. Gill, "Comparison of wave height measurement algorithms for ship-borne x-band nautical radar," *Can. J. Remote Sens.*, vol. 42, no. 4, pp. 343–353, 2016.
[35] G. V. Weinberg, L. Bateman, and P. Hayden, "Development of non-coherent CFAR detection processes in Weibull background," *Digit. Signal Process.*, vol. 75, pp. 96–106, 2018.
[36] P. Mukhopadhyay and B. B. Chaudhuri, "A survey of Hough transform," *Pattern Recognit.*, vol. 48, no. 3, pp. 993–1010, 2015.
[37] Q. Cheng, X. Wu, X. Zhang, and Q. Yang, "A novel sea clutter suppression method based on SVD-FRFT at low signal-to-clutter ratio," *Electron. Lett.*, vol. 59, no. 14, 2023, Art. no. 12874.
[38] Z. Chen, C. He, C. Zhao, and F. Xie, "Using SVD-FRFT filtering to suppress first-order sea clutter in HFSWR," *IEEE Geosci. Remote Sens. Lett.*, vol. 14, no. 7, pp. 1076–1080, 2017.
[39] B. Zhang, J. Zhou, J. Xie, and W. Zhou, "Weighted likelihood CFAR detection for W background," *Digit. Signal Process.*, vol. 115, 2021, Art. no. 103079.
[40] K. Zebiri and A. Mezache, "Triple-order statistics-based CFAR detection for heterogeneous Pareto type I background," *Signal Image Video Process.*, vol. 17, no. 4, pp. 1863–1703, 2023.
[41] K. Zebiri and A. Mezache, "Radar CFAR detection for multiple-targets situations for Weibull and log-normal distributed clutter," *Signal Image Video Process.*, vol. 15, pp. 1671–1678, 2021.

Zhizhong Lu received the B.Sc. degree in radio electronics from Fudan University, Shanghai, China, in 1989, and the M.Sc. and Ph.D. degrees in navigation guidance from Harbin Engineering University, Harbin, China, in 2001 and 2008, respectively.

He is currently a Professor with the College of Automation, Harbin Engineering University. His main research interests include marine integrated hydrological remote sensing and information forecasting technology.

Baotian Wen received the B.Sc. degree in automation in 2017 from Harbin Engineering University, Harbin, China, where he is currently working toward the Ph.D. degree in instrument science and technology.

His research interests include marine radar image processing, signal processing and target detection.

Yongfeng Mao received the M.A.Sc. degree in instrument science and technology from Harbin Engineering University, Harbin, China, in 2024.

His research interests include marine radar image processing and target detection.

Bowen Zhou received the B.Sc. degree in mechatronics engineering from Beijing Jiaotong University, Beijing, China, in 2019. He is currently working toward the Ph.D. degree in instrument science and technology with Harbin Engineering University, Harbin, China.

His research interests include marine radar image processing and target detection.